RSC Advances

PAPER

View Article Online
View Journal | View Issue

Cite this: *RSC Adv.*, 2025, **15**, 31917

Porous polysiloxane MWCNT nanocomposites for high-performance and scalable triboelectric nanogenerators

Orkhan Gulahmadov, *[ab] Lala Gahramanli, [a] Mustafa Muradov,[a] Nahida Musayeva, [c] Stefano Bellucci,[d] Nadia Todorova[e] and Christos Trapalis[e]

In this study, porous polysiloxane (PS)/multi-walled carbon nanotube (MWCNT) nanocomposite films were developed as high-performance triboelectric layers for flexible triboelectric nanogenerators (TENGs). TENGs convert mechanical motion into electricity and offer a promising solution for self-powered electronic systems. The nanocomposites were fabricated using a doctor blading method, and porosity was introduced *via* a simple, scalable salt-leaching technique. Sieved salt particles of varying sizes produced films with fine, medium, and large pores. Raman spectroscopy confirmed uniform MWCNT dispersion and strong interfacial interaction within the PS matrix. SEM analysis verified controlled pore morphology. Dielectric measurements showed reduced permittivity with increasing pore size due to air void incorporation. Triboelectric performance improved significantly with porosity; the medium porosity sample exhibited the best output with an open-circuit voltage of 65 V, short-circuit current of 6.9 μA, and a power density of 280.6 mW m^{-2}. This enhancement is attributed to the optimized combination of surface roughness, contact area, and dielectric behavior, promoting efficient charge generation and transfer. These results highlight the potential of microstructural engineering in porous nanocomposites for next-generation energy harvesting applications.

Received 11th August 2025
Accepted 28th August 2025

DOI: 10.1039/d5ra05894e

rsc.li/rsc-advances

1. Introduction

As our world becomes more connected through wearable devices, wireless sensors, and smart technologies, the need for lightweight, flexible, and sustainable energy sources continues to increase.[1–4] Triboelectric nanogenerators (TENGs) have emerged as a promising solution, capable of converting everyday mechanical motions – such as walking, tapping, or subtle vibrations—into usable electrical energy,[5–10] and recent studies have highlighted their applications in water splitting, wind, and wave energy harvesting.[11–13] Their simple design, low cost, and ability to work with a wide range of materials make TENGs an appealing option for powering small electronics, especially in remote or off-grid settings.[14–18]

The performance of a TENG mainly depends on the materials used in its fabrication.[19–24] PS, a soft and stretchable polymer, is commonly used because of its durability and flexibility.[9,10,22,25–27] However, a challenge with polysiloxane is its relatively low dielectric permittivity, which limits how much electrical charge it can store and transfer during contact.[28–31] To improve this, researchers have investigated adding conductive nanomaterials, such as MWCNTs, to create nanocomposites that boost charge trapping and overall electrical response.[32–37] Conductive nanofillers like MWCNTs can form localized micro-capacitor structures, known as the nanocapacitor effect, within the polymer matrix. These nanoscale capacitive networks enhance charge storage, interfacial polarization, and dielectric response, leading to improved triboelectric performance. Several studies have confirmed this mechanism, demonstrating that filler distribution and nanocapacitor formation significantly increase TENG output efficiency.[38–40]

Another effective method to boost TENG output is adding porosity to the triboelectric layer. Introducing air-filled pores increases surface roughness, improves the actual contact area, and changes dielectric properties in ways that favor triboelectric charge generation.[22,41–43] Although various techniques have been suggested to create porosity, many require complex equipment or lack precise control of pore structure.[22,43–47]

In this study, we introduce a simple, controllable, and cost-effective method for fabricating porous PS/MWCNT nanocomposite films using salt leaching technique. Uniformly sieved salt particles were manually sprayed onto the surface of the uncured polymer, serving as a sacrificial porogen. Following

[a]*Nano Research Laboratory, Center of Excellence, Baku State University, Academic Zahid Khalilov St. 23, Baku, AZ1148, Azerbaijan. E-mail: ogulahmadov@bsu.edu.az*
[b]*Faculty of Engineering, Karabakh University, Khankendi, AZ2600, Azerbaijan*
[c]*Institute of Physics, Ministry of Science and Education of Azerbaijan, Baku, Azerbaijan*
[d]*National Institute of Materials Physics, Atomistilor Str. 405 A, 077125, Bucharest-Magurele, Romania*
[e]*Institute of Nanoscience and Nanotechnology, National Center for Scientific Research "Demokritos", Agia Paraskevi, 15341, Greece*

the curing process, the salt was removed by leaching, resulting in a porous structure with tunable pore sizes. This approach enables systematic control over the microstructure of composite films. The influence of pore size on dielectric properties was comprehensively investigated and shown to have a direct impact on the electrical performance of the resulting TENG devices. This combined strategy of nanofiller reinforcement and tailored porosity offers a scalable route for optimizing TENG materials and holds significant promise for the development of high-performance, flexible energy harvesting systems for real-world applications.

2. Materials and methods

2.1. Materials

MWCNTs were obtained from Southwest NanoTechnologies (SWeNT, Norman, OK, USA). Ethanol (≥95.0% purity) was purchased from Merck (Darmstadt, Germany) and used as a dispersion medium. Nylon was sourced from commercially available nylon socks made of 90% nylon and 10% other polymers, with an average thread diameter of 43 μm. These nylon threads served as the positive triboelectric material due to their strong electron-donating properties.[48,49] For the negative triboelectric layer, polysiloxane (Xinus Silicone Parts 20A and 20B) was chosen because of its high negative triboelectric polarity, excellent mechanical flexibility, and strong electron affinity. These qualities make polysiloxane an effective material for charge generation and transfer when paired with nylon. Besides its favorable triboelectric properties, polysiloxane offers benefits such as low cost, commercial availability, and ease of processing, making it suitable for flexible TENG fabrication.[33,50] Aluminum foil (SoftyME, 10 μm thick) was used as the electrode material to collect and transfer electrical signals generated during TENG operation. All materials were used as received unless otherwise specified.

2.2. Functionalization of MWCNTs and preparation of 0.05 wt% Ethanol/MWCNT mixture

2.2.1. Functionalization process. MWCNTs were first purified using 30% nitric acid (HNO_3) (Carlo Erba, Milan, Italy) and deionized (DI) water. After purification, 100 mg of MWCNTs were subjected to oxidative treatment by mixing with 4 mL of 65% HNO_3 and 12 mL of 93.6–95.6% sulfuric acid (H_2SO_4) (AO Base No. 1 Chemical Reagents, Moscow, Russia). The mixture was placed in a glass vessel and ultrasonicated at 68 kHz while maintaining a temperature of 50 °C for 3 hours. After the reaction, 500 mL of DI water was added to dilute the mixture, and the suspension was allowed to stabilize for 12 hours. The resulting product was filtered under vacuum and thoroughly washed with DI water until a neutral pH was reached. Finally, the functionalized MWCNTs were dried in an oven at 40 °C for 24 hours. The presence of oxygen-containing functional groups on the MWCNTs was confirmed by Fourier-transform infrared spectroscopy using an IR Affinity-1 spectrometer (Shimadzu, Kyoto, Japan).[33]

2.2.2. Preparation of 0.05 wt% Ethanol/MWCNT dispersion. As shown in Fig. 1a, functionalized multi-walled carbon nanotubes (f-MWCNTs) were precisely weighed and dispersed in ethanol to prepare the nanofiller solution for incorporation into the PS matrix. Specifically, 0.005 g of f-MWCNTs was added to 10 mL of ethanol, yielding a 0.05 wt% concentration relative to the total mass of the ethanol/f-MWCNT mixture. This concentration was selected based on both literature precedents, which demonstrates that 0.05 wt% is effective for enhancing triboelectric and dielectric performance in polymer/MWCNT systems,[33,51] and our own optimization studies on PS/MWCNT composites. In our experiments, 0.01, 0.03, 0.05, and 0.1 wt% f-MWCNT concentrations were tested, and 0.05 wt% was found to provide the best balance of electrical output, dielectric enhancement, and material homogeneity, making it the optimal choice for the present study.

To ensure effective dispersion and minimize the agglomeration of nanotubes—commonly caused by strong van der Waals interactions—each mixture was subjected to ultrasonication for 1 hour using a high-power probe sonicator operating at 500 W and 20 kHz. This process effectively breaks nanotube bundles and facilitates the formation of a stable, homogeneous suspension, which is essential for uniform integration into the polysiloxane matrix during subsequent film fabrication steps.

2.3. Fabrication of 0.05 wt% PS/MWCNT nanocomposites using the doctor blading method

The PS/MWCNT nanocomposite films were prepared using the doctor blading method, a widely used and cost-effective technique for fabricating thin films with uniform thickness.[52–54] This method is particularly advantageous due to its simplicity, scalability, and ability to precisely control film thickness by adjusting the blade gap. It also allows for rapid deposition over large areas and is compatible with a variety of substrates and viscous materials, making it highly suitable for flexible electronic applications such as TENGs.[55,56]

In this study, we focused on fabricating nanocomposites containing 0.05 wt% f-MWCNTs, a concentration previously found to provide favorable performance characteristics. To begin with, equal amounts of the two components of the polysiloxane system (Xinus Silicone Parts 20A and 20B) were mixed in a 1 : 1 weight ratio, as recommended by the manufacturer. The mixture was stirred thoroughly for 10 minutes to ensure a homogeneous and bubble-free base matrix.

In parallel, 0.05 wt% of f-MWCNTs (relative to the total weight of the ethanol/MWCNT dispersion) were dispersed in ethanol and sonicated to improve dispersion quality. This dispersion was then slowly added to the polysiloxane mixture, followed by vigorous stirring for 15 minutes to ensure uniform distribution of the nanotubes throughout the polymer network. The resulting nanocomposite was cast onto clean aluminum foil, which served both as the substrate and the bottom electrode in the final TENG device. A doctor blade with a fixed gap of 200 μm was used to spread the mixture, resulting in a uniform and controlled film thickness. The coated films were allowed to dry at room temperature for 48 hours, ensuring complete

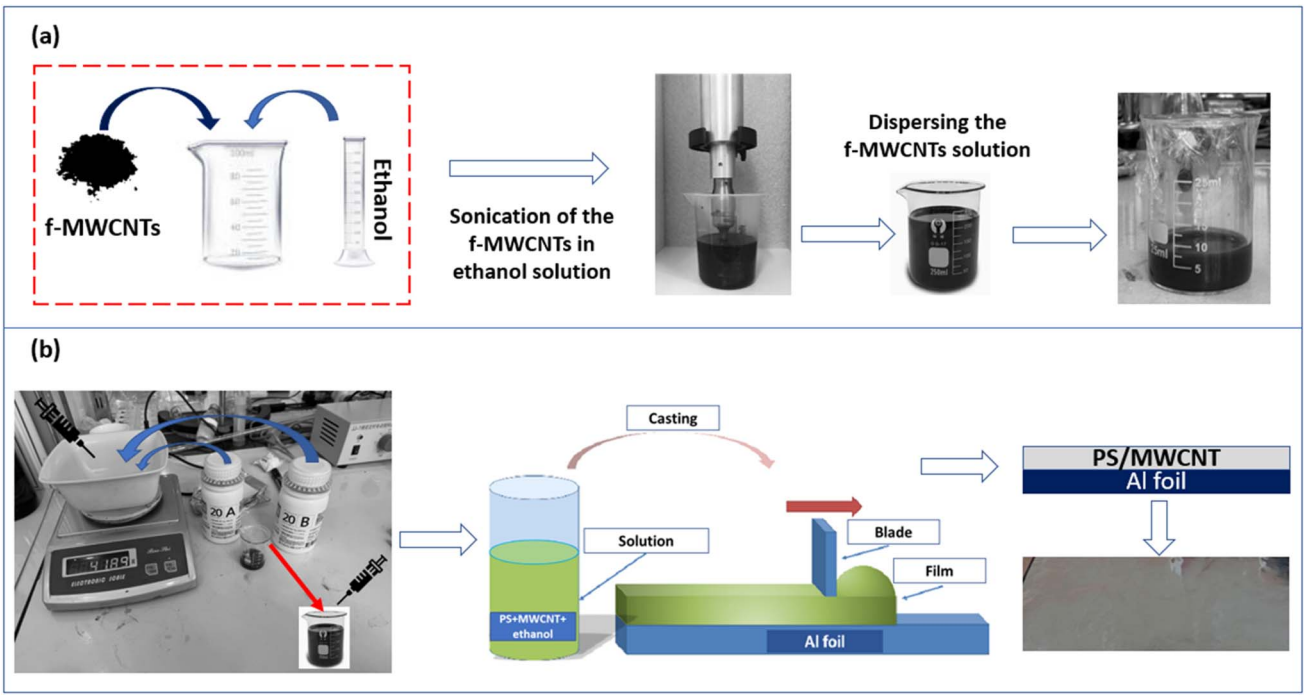

Fig. 1 (a) Preparation of functionalized f-MWCNT dispersions in ethanol at a concentration of 0.05 wt% using probe ultrasonication; (b) schematic illustration of the fabrication process of PS/MWCNT nanocomposite films *via* the doctor blading method.

solvent evaporation and promoting a smooth, defect-free surface.

After curing, the nanocomposite films were gently peeled off the aluminum foil and cut into 4 cm × 4 cm squares for device assembly. The final thickness of the films was measured to be approximately 190 μm, with minor variation across samples. For comparison, a reference sample composed of non-porous PS/MWCNT nanocomposite film was prepared using the same method. This allowed for a direct evaluation of the impact of MWCNT incorporation on the dielectric and triboelectric behavior of the fabricated TENGs.

This approach demonstrates that the doctor blading technique is not only versatile and easy to implement but also highly effective for fabricating reproducible, high-quality nanocomposite films for energy harvesting applications.

2.4. Fabrication of porous structure on the surface of PS/MWCNT nanocomposite by using salt leaching method

As illustrated in Fig. 2, surface porosity in the PS/MWCNT nanocomposite films was introduced using the salt leaching method, in which uniformly sieved salt crystals served as sacrificial porogens.[57] The salt particles were manually and evenly distributed onto the surface of the uncured polymer. After thermal curing, the films were immersed in deionized water to dissolve and remove the salt, resulting in a porous surface structure. Owing to the hydrophobic nature of the polysiloxane matrix, water selectively dissolved the salt without compromising the integrity of the composite. A key advantage of this approach over conventional templating methods is its simplicity, scalability, and cost-effectiveness.[58] The salt-leaching method requires no complex equipment and can be easily applied to large-area films, making it suitable for practical and scalable fabrication of porous nanocomposites. Additionally, the pore size and distribution can be precisely tuned by selecting salt particles of different sizes, enabling systematic control over the film microstructure.

To control the pore sizes, we used three distinct salt crystal ranges: fine salt with crystals between 10 and 50 micrometers, medium salt ranging from 100 to 300 micrometers, and large salt crystals between 300 and 1000 micrometers. The salt was gently sprinkled by hand onto freshly cast nanocomposite films from a height of about 10 cm, as illustrated in Fig. 2. Gravity caused the salt crystals to lightly embed into the soft PS/MWCNT surface.

After sprinkling, the samples were left to dry at room temperature for two days, allowing the films to fully set. The surfaces were then thoroughly washed with distilled water. As the salt dissolved and washed away, it left behind a porous surface that closely reflected the size and distribution of the original salt crystals. This straightforward yet effective method enabled us to create well-controlled porous structures on the nanocomposite surface, enhancing surface area and potentially improving the performance of devices such as TENGs.

2.5. Fabrication of TENGs based on nylon and porous PS/MWCNT nanocomposites

Nylon was chosen as the positive triboelectric material in the fabrication of the TENG due to its advantageous position in the triboelectric series, which allows it to effectively donate electrons. As a synthetic polyamide, nylon combines excellent

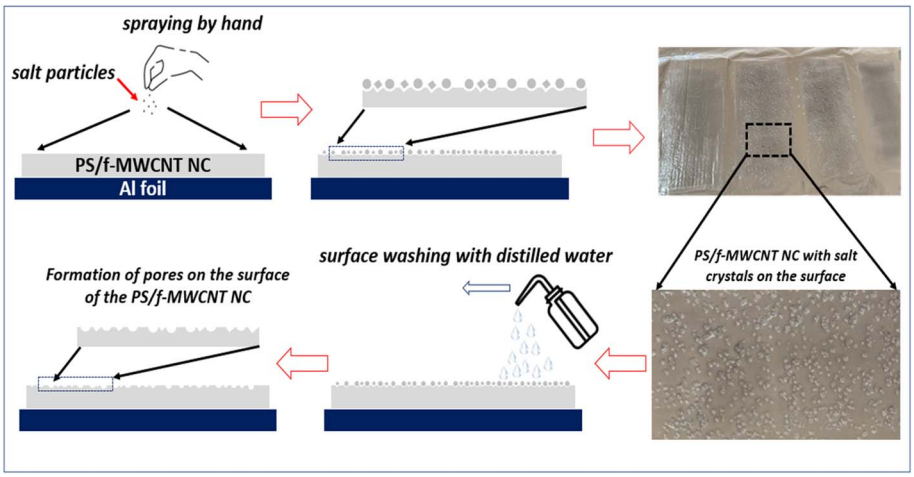

Fig. 2 Schematic illustration of the porous surface fabrication process on PS/MWCNT nanocomposite films.

mechanical flexibility and chemical stability with a strong ability to generate surface charges during frictional contact. These qualities make it a popular choice in triboelectric nanogenerators, as it improves charge transfer and maintains durability under repeated mechanical stress.

In this study, the nylon film (shown in Fig. 3a) is composed of a tightly woven mesh of fibers, forming a porous and flexible structure. SEM analysis indicated that the individual fiber diameters average around 44 μm. This fibrous architecture increases the effective contact surface area, thereby enhancing charge generation when paired with a negative triboelectric material like polysiloxane.

As shown in Fig. 3b, preparing the triboelectric layer, the nylon film was laminated onto aluminum foil using a thin, electrically conductive double-sided tape, ensuring strong mechanical adhesion while maintaining a continuous electrical conduction pathway. The aluminum foil thus effectively serves as the bottom electrode, allowing electrons generated in the nylon layer to flow during TENG operation. The resulting nylon–aluminum composites were then cut into uniform squares of 4

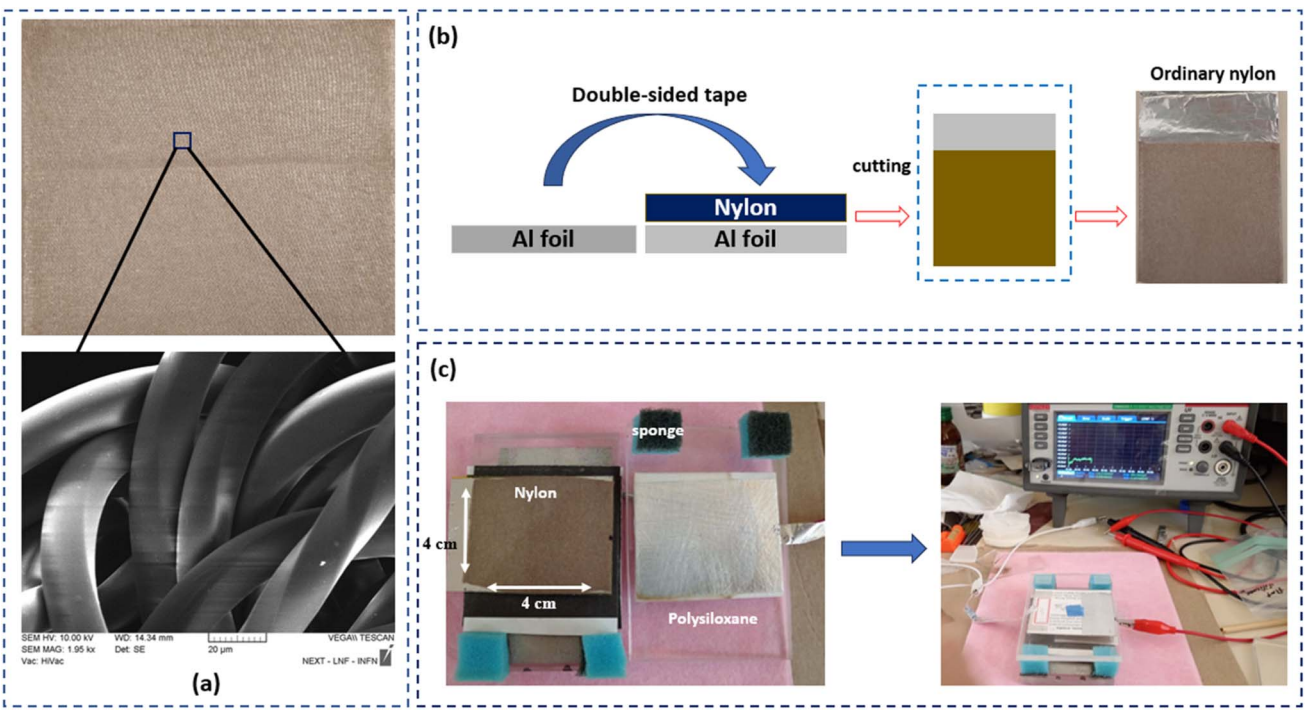

Fig. 3 (a) Microscopic image of the nylon film illustrating its fibrous network with an average fiber diameter of approximately 44 μm; (b) preparation step showing the nylon film laminated onto aluminum foil using double-sided adhesive; (c) schematic of the TENG fabrication process combining nylon and either non-porous polysiloxane/MWCNT nanocomposite films or porous polysiloxane/MWCNT nanocomposite films.

× 4 cm to standardize the contact area across devices. These prepared nylon electrodes were then combined with either non-porous PS/MWCNT nanocomposite films or porous PS/MWCNT nanocomposite films to assemble the full TENG devices, as shown in Fig. 3c. The effective combination of nylon as the positive triboelectric layer with polysiloxane-based nanocomposite films creates a significant triboelectric potential difference, which is crucial for enhancing the electrical output of the TENG during cyclic mechanical operation.

2.6. Characterization methods

Raman spectroscopy was performed using an EnSpectr R532 Raman spectrometer (Enhanced Spectrometry Inc., Poland), equipped with a 532 nm excitation laser, to analyze the molecular structure and interactions within the PS/MWCNT nanocomposite films. SEM was conducted using an FEI Quanta Inspect microscope (FEI, Hillsboro, OR, USA) equipped with a tungsten filament, operating at an accelerating voltage of 25 kV. The dielectric properties of the polysiloxane/MWCNT nanocomposite films were measured using an Immittance Meter E7-20 across a wide frequency spectrum from 60 Hz to 1 MHz, enabling analysis of the frequency-dependent dielectric constant.

2.7. Measurement of the performance of the TENG

To assess the impact of surface porosity on the performance of TENGs, both non-porous and porous PS/MWCNT nanocomposite films were employed as the negative triboelectric layers, while nylon served as the positive counterpart. All films were precisely cut into 4 × 4 cm^2 sections for device assembly. The TENG devices were fabricated by placing the nylon film in direct contact with the polysiloxane-based layer, maintaining a fixed separation gap of 25 mm between the triboelectric surfaces. Electrical outputs were measured using a digital multimeter (DMM6500 $6\frac{1}{2}$-digit, Keithley) under an approximate contact–separation frequency of 2 Hz. The measurements were performed manually, with approximately 120 contact–separation cycles applied per minute. Care was taken to maintain consistency in applied force and frequency across all trials, ensuring reproducibility of the results. Experiments were conducted at controlled environmental conditions of 31 °C and 50% relative humidity to ensure repeatability and reliability.

Environmental factors such as humidity and temperature play a significant role in TENG performance.[22,33,50] Elevated humidity levels facilitate moisture adsorption on the triboelectric surfaces, increasing surface conductivity and accelerating charge dissipation, thereby reducing the device's electrical output. Conversely, lower humidity levels promote charge retention, enhancing output performance. Temperature fluctuations influence the dielectric properties and mechanical compliance of the polymer layers, which in turn affect charge generation and separation efficiency. The chosen separation gap of 25 mm was optimized to balance the air breakdown threshold and charge transfer efficiency; excessive gap distances diminish electrostatic induction and reduce output, while overly small gaps increase the risk of premature discharge and device instability.

3. Results and discussion

3.1. Raman spectroscopy

Raman spectroscopy was used as a non-destructive method to examine the structural features and chemical interactions in both pristine polysiloxane and its nanocomposites containing MWCNTs. Fig. 4 shows the Raman spectra for both sample types. As expected, the spectra are mainly influenced by the vibrational features of the polysiloxane matrix, which can be attributed to the naturally weak Raman scattering cross-section of CNTs, reported to be about 45 times lower than that of polysiloxane.[59]

Characteristic vibrational modes associated with methyl groups were observed in both spectra. Peaks at 2962 cm^{-1} and 2908 cm^{-1} correspond to the asymmetric and symmetric stretching vibrations of $-CH_3$ groups, respectively. Bending vibrations of $-CH_3$ are reflected in the bands at 1403 cm^{-1} and 1257 cm^{-1}. Additionally, CH_3 rocking modes were identified at 860 cm^{-1} and 784 cm^{-1}.[60,61] Prominent signals located at 703 cm^{-1} and 485 cm^{-1} are attributed to the symmetric stretching of the Si–O–Si backbone, while the bands at 190 cm^{-1} and 160 cm^{-1} correspond to wagging and twisting motions within the polysiloxane network. These features confirm the structural integrity of the PS framework in both pristine and composite films.

In the PS/MWCNT nanocomposites, these bands not only persist but exhibit slightly increased intensity, which may suggest improved polymer–filler interaction and enhanced dispersion of CNTs throughout the matrix. Notably, a weak shoulder emerging around 1583–1615 cm^{-1} corresponds to the G band of CNTs, indicative of in-plane stretching vibrations of sp^2-hybridized carbon atoms within graphitic domains.[36,62] This band serves as a fingerprint of graphitic ordering and is generally associated with well-aligned carbon nanotube structures.

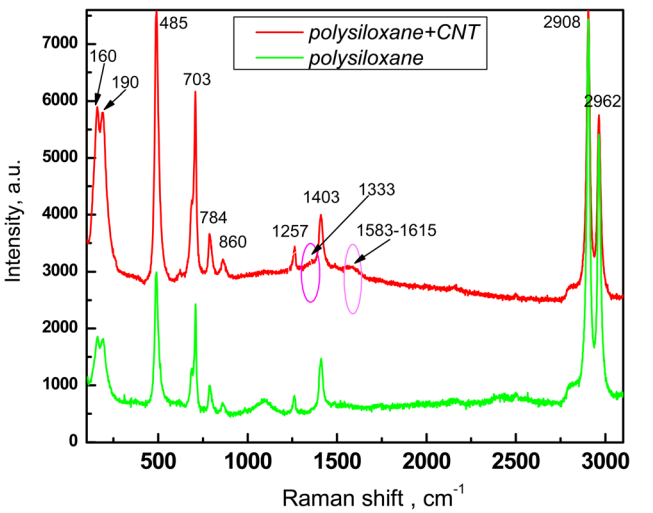

Fig. 4 Raman spectra of pristine PS and PS/CNT nanocomposite films.

A subtle yet distinguishable peak near 1333 cm^{-1}, corresponding to the D band, appears only in the composite spectrum. The D band arises due to the presence of structural defects or disruptions in the symmetry of the sp^2 carbon lattice. It is typically used as an indicator of disorder or functionalization within carbon-based nanostructures. The weak intensity of this band in the composite suggests a low level of defect sites on the CNT surface, consistent with effective functionalization and minimal disruption during processing.

Collectively, the Raman spectra confirm the successful incorporation of MWCNTs into the PS matrix and indicates that the nanotubes are uniformly dispersed with minimal structural degradation. These findings also support the hypothesis of improved interfacial compatibility between the polymer and nanofiller, which contributes to the enhanced electrical and dielectric properties observed in the nanocomposite-based TENGs.

3.2. SEM

As shown in Fig. 5, the surface morphology of the f-MWCNTs was characterized by SEM and operated at an accelerating voltage of 25 kV. Representative micrographs were obtained at a magnification of 800 00×, with a working distance of 9.9 mm and a horizontal field width of 3.38 μm, employing secondary electron mode to enhance surface detail contrast.

The SEM images reveal a highly entangled network of f-MWCNTs displaying uniform, elongated tubular morphology, with outer diameters ranging from approximately 117 to 145 nm, consistent with dimensions reported for acid-functionalized MWCNTs in the literature. The nanotubes exhibit excellent dispersion with negligible aggregation, underscoring the effectiveness of the functionalization process in preserving the structural integrity of the nanotubes while enhancing their dispersibility.

This well-dispersed and interconnected morphology implies improved interfacial compatibility and interaction potential, which are critical for the homogeneous incorporation of f-MWCNTs into polymer matrices. The preserved cylindrical structure and minimal aggregation are anticipated to facilitate efficient interfacial charge transfer, thereby enhancing the electrical and dielectric properties of the resulting nanocomposites, particularly for triboelectric applications.

The surface morphology of the porous PS/MWCNT nanocomposite, fabricated *via* the salt leaching method was analyzed using SEM, as shown in Fig. 6. SEM images show that the pores can be clearly controlled in size and distribution by adjusting the salt particle size. This demonstrates the versatility and reproducibility of the salt-leaching approach, providing a practical advantage over conventional templating methods that often require complex equipment or offer limited control over pore morphology. The low-magnification SEM image (Fig. 6a, 50×) demonstrates a well-distributed porous structure across the nanocomposite surface. Pores appear predominantly elliptical or irregularly circular, with a relatively uniform spatial distribution. This uniformity directly reflects the effectiveness of the salt crystal leaching method, where crystals of various sizes – sprinkled onto the soft PS/MWCNT film – acted as removable porogens.

The high-magnification image (Fig. 6b, 200×) provides further insight into the individual pore characteristics. Measured pore diameters range from approximately 196 μm to 236 μm, which aligns well with the medium-sized salt crystals (100–300 μm) used during fabrication. The sharp, well-defined pore walls indicate effective removal of salt and minimal matrix deformation during the washing and drying processes. This suggests good dimensional stability of the PS matrix and strong interfacial integrity, even post-processing.

Notably, fibrous or filament-like structures are visible within the matrix, which are attributed to the partial exposure or pull-out of f-MWCNTs their presence confirms the successful incorporation and surface integration of MWCNTs, which is critical for enhancing the nanocomposite's mechanical strength, electrical conductivity, and surface activity. The porous architecture significantly increases surface area, which is particularly advantageous for applications such as TENGs, where interfacial contact and charge transfer are critical.

In summary, the SEM images validate that the salt leaching approach yielded a porous PS/MWCNT nanocomposite with

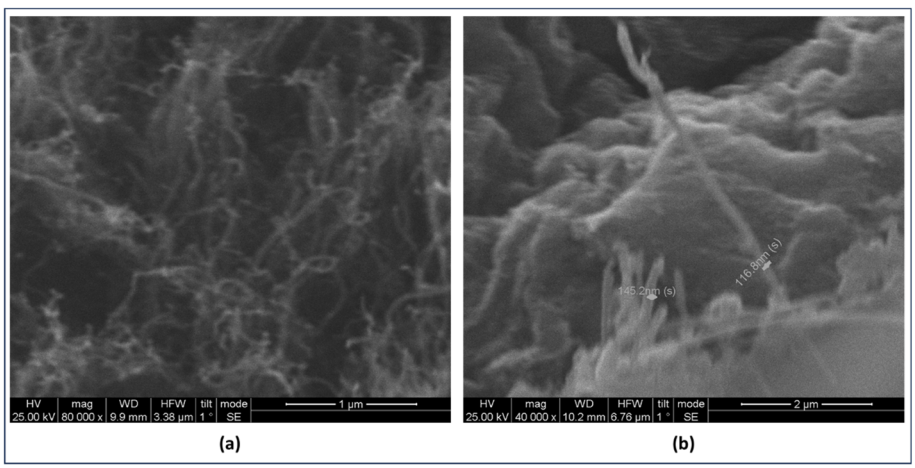

Fig. 5 SEM images of f-MWCNTs at (a) 400 00× and (b) 800 00× magnifications showed well-dispersed, uniform nanotubes.

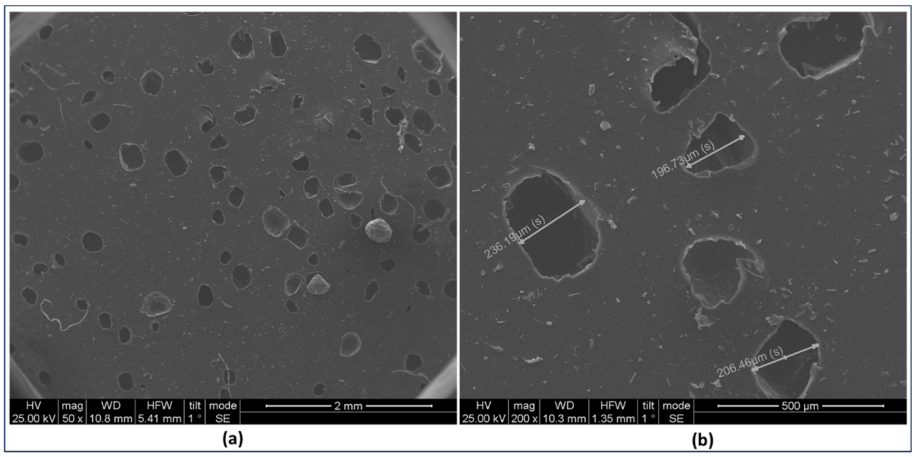

Fig. 6 SEM images of porous PS/MWCNT nanocomposite surfaces: (a) uniformly distributed pores (50×); (b) macropores (~196–236 μm) formed by medium-sized salt crystals (200×).

controllable pore size and distribution. The observed microstructural features support the material's potential for use in multifunctional surface-based devices.

3.3. Influence of pore size on the dielectric behavior of PS/MWCNT nanocomposites

Fig. 7 presents the frequency-dependent dielectric permittivity (ε') of PS/MWCNT nanocomposites with varying porosity levels. The samples were categorized as non-porous (ordinary), fine-porous, medium-porous, and large or big-porous based on the size of the sacrificial salts or sugar powders used during fabrication. Dielectric measurements were performed across the full frequency range accessible by the instrument (60 Hz–1 MHz) using the Immittance Meter E7-20. The x-axis represents lg ω, the base-10 logarithm of angular frequency (rad s^{-1}), where lg 7 = 10^7 rad s^{-1}.

For clarity, only the low-frequency region (>1 kHz) is shown in Fig. 7, as interfacial polarization and dipolar relaxation dominate the dielectric response in this range. Frequencies below 1 kHz show minimal variation and primarily noise-like contributions, which do not provide meaningful insight into the polarization mechanisms. This focus is consistent with previous studies in the literature on polymer–nanotube composites.[33,48–51]

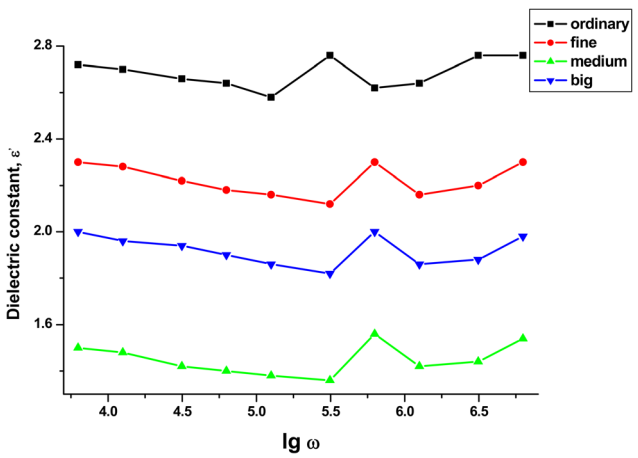

Fig. 7 Dielectric constant of PS/MWCNT nanocomposites with different porosity levels over a range of frequencies.

The results reveal that interfacial polarization between carbon nanotubes and the polysiloxane matrix governs the dielectric behavior, leading to measurable changes in the dielectric constant. Variations among non-porous, fine-porous, medium-porous, and big-porous composites underscore the impact of pore structure on dielectric properties and, consequently, on the triboelectric performance of the nanogenerators.

The data show a steady decline in dielectric permittivity as porosity increases. The non-porous PS/MWCNT nanocomposite displays the highest ε' values, while the highly porous PS/MWCNT nanocomposite shows the lowest, highlighting the significant influence of porosity on dielectric properties. This decrease is mainly due to the presence of air voids within the polymer matrix. Since air has an extremely low dielectric constant ($\varepsilon_{air} \approx 1$), it effectively reduces the overall dielectric polarization of the material.[63,64]

To quantitatively interpret this behavior, we consider the Maxwell–Garnett effective medium approximation,[65–67] which models the dielectric constant of a composite material comprising a matrix and inclusions:

$$\varepsilon_{eff} = \varepsilon_m \left(\frac{2\varepsilon_m + \varepsilon_i + 2f(\varepsilon_i - \varepsilon_m)}{2\varepsilon_m + \varepsilon_i - f(\varepsilon_m - \varepsilon_i)} \right) \quad (1)$$

where ε_{eff} – is the effective dielectric permittivity of the porous composite, ε_m – is the dielectric constant of the matrix (*i.e.*, PS/MWCNT), ε_i – is the dielectric constant of the inclusion (*i.e.*, air ≈ 1), and f is the volume fraction of the pores. This model predicts that as the pore volume fraction increases, the effective dielectric constant ε_{eff} decreases nonlinearly. Additionally, larger pores typically contribute to higher local void volume, thus amplifying the reduction in permittivity, consistent with the experimental observations.

All samples show typical dielectric dispersion: ε' slightly decreases with increasing frequency, especially at lower frequencies (lg ω < 5.5). This pattern results from dipolar polarization relaxation, where molecular dipoles and interfacial charges cannot quickly align with high-frequency fields. Notably, a small rise in ε' around lg $\omega \approx$ 5.7–6.0 in all samples indicates the presence of Maxwell–Wagner–Sillars (MWS) interfacial polarization, which occurs at the interfaces between the PS matrix, MWCNTs, and pores.

The fine- and medium-porous samples show intermediate dielectric performance, suggesting that the tuning of pore size and volume fraction allows for control modulation of the dielectric constant in such nanocomposites.

Interestingly, as the porosity of the PS/MWCNT nanocomposites increases, the local peak associated with interfacial polarization shifts toward higher frequencies. This behavior can be attributed to the reduced effective permittivity and conductivity of the composite with increasing pore volume, which shortens the relaxation time of MWS polarization. According to relation (2), a decrease in both ε and σ results in faster interfacial polarization dynamics, thereby shifting the polarization response to higher frequencies.

$$\tau = \frac{\varepsilon_{\text{eff}}}{\sigma_{\text{eff}}} \quad (2)$$

where τ – relaxation time, σ_{eff} is the effective electrical conductivity of the system. Additionally, the disruption of continuous interfacial networks by pores further contributes to the earlier onset of dielectric relaxation.

In conclusion, the incorporation of pores into PS/MWCNT nanocomposites significantly influences their dielectric performance. The observed decrease in permittivity with increasing porosity is consistent with predictions from effective medium theory and highlights the importance of microstructural control in designing advanced dielectric materials.

3.4. Output performance of TENGs based on porous PS/MWCNT nanocomposites

As illustrated in Fig. 8, the designed TENG is fabricated with a multilayer configuration consisting of a nylon film and a PS/MWCNT nanocomposite film as the triboelectric layers. Aluminum foil serves as the conductive electrode, while a cardboard (carton paper) layer provides mechanical support. Nylon, positioned high in the triboelectric series and exhibiting excellent flexibility, functions as the positively charged material. In contrast, the PS/MWCNT composite—whether non-porous or porous—acts as the negatively charged triboelectric layer due to its strong electron affinity. To systematically investigate the influence of porosity, four different TENG configurations were fabricated, incorporating non-porous and porous PS/MWCNT nanocomposite films with varying pore sizes.

The operational mechanism of the device follows a vertical contact–separation mode, schematically represented in Fig. 8, and consists of four stages. In Stage 1, the application of mechanical force brings the two triboelectric layers into contact. Due to their differing electron affinities, triboelectric charges are generated at the interface: electrons transfer from nylon to the PS/MWCNT layer, resulting in positive and negative charges on their respective surfaces. In Stage 2, the release of the applied force allows a sponge element at the device edges to facilitate the mechanical separation of the layers. This

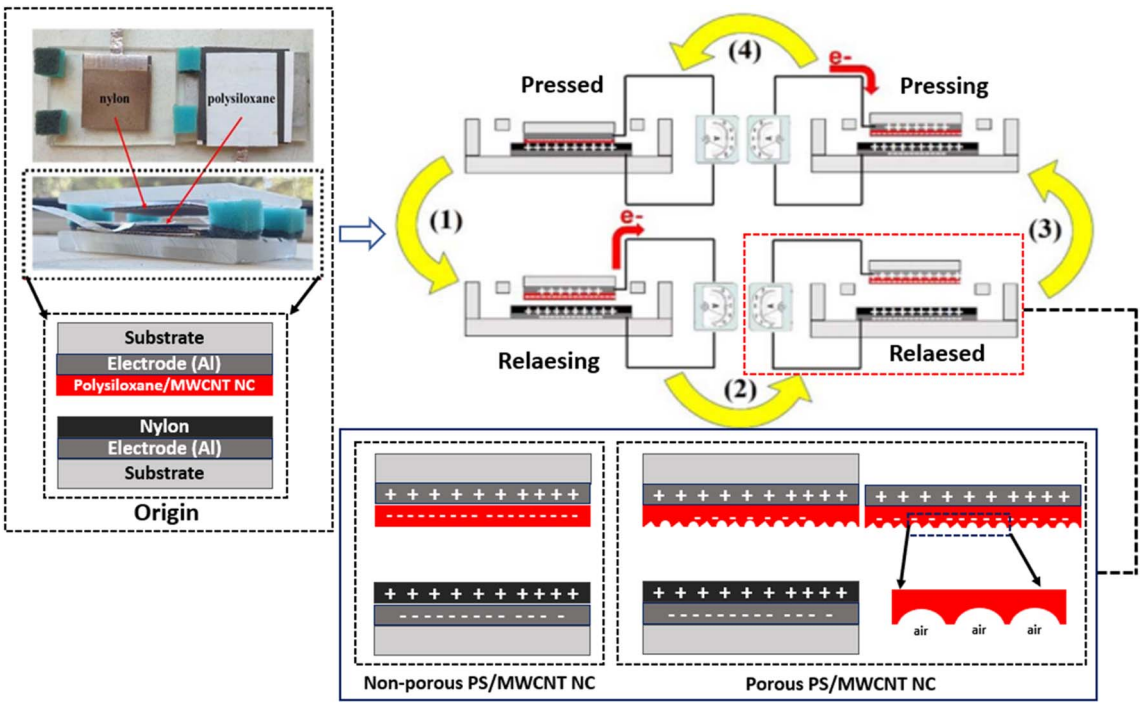

Fig. 8 Working principle of the nylon and PS/MWCNT nanocomposite-based TENG, showing contact, charge transfer, separation, and neutralization stages during mechanical motion.

separation induces an electric potential difference between the electrodes, causing electrons to flow through the external circuit by electrostatic induction, thus generating a current.

In Stage 3, as the separation distance reaches its maximum, the potential difference across the electrodes also peaks, leading to maximum output voltage and current. The induced charge is directly related to the surface charge density and the effective distance between the layers. In Stage 4, reapplication of force returns the layers into contact, enabling the recombination or neutralization of triboelectric charges and reversing the electron flow direction, thereby producing an alternating current (AC) output.

Crucially, in the case of porous nanocomposite films, the presence of air-filled voids within the PS matrix introduces additional interfacial sites between air (which is weakly triboelectric and positively charged) and the negatively charged polysiloxane. This internal air–polysiloxane interface contributes to the triboelectric effect by enabling additional charge separation and electrostatic induction beyond the primary contact surface. The air pockets within the pores also modify the local dielectric environment and enhance the surface roughness, thereby increasing the real contact area during compression and improving the efficiency of charge transfer. As a result, the integration of porosity not only alters the mechanical compliance and dielectric properties of the triboelectric layer but also introduces new mechanisms of charge generation, significantly boosting the overall output performance of the TENG.[45,68–71]

This combination of surface morphology tuning, enhanced dielectric response, and air–polymer interfacial polarization in porous structures validates the strategy of pore engineering as an effective approach to optimize energy harvesting efficiency in TENG devices.[22]

The triboelectric output performance of the fabricated TENGs was systematically evaluated using nanocomposite films with varying degrees of porosity, achieved through a salt leaching method applied to PS/MWCNT structures. The key output parameters measured included the maximum open-circuit voltage (V_{oc}), short-circuit current (I_{sc}), power, and power density—each serving as a fundamental metric for assessing the energy harvesting capability of the devices.

As summarized in Fig. 9, a clear enhancement in output performance was observed with the introduction of porosity into the nanocomposite matrix. As shown in Fig. 9a and c, the TENG based on the non-porous PS/MWCNT film exhibited a maximum voltage of 40 V and a current of 4.9 μA under identical mechanical actuation conditions. These values serve as a reference point, illustrating the limitations associated with dense, unstructured dielectric films in triboelectric applications.

In comparison, TENGs fabricated using porous nanocomposites showed significantly improved electrical output. As

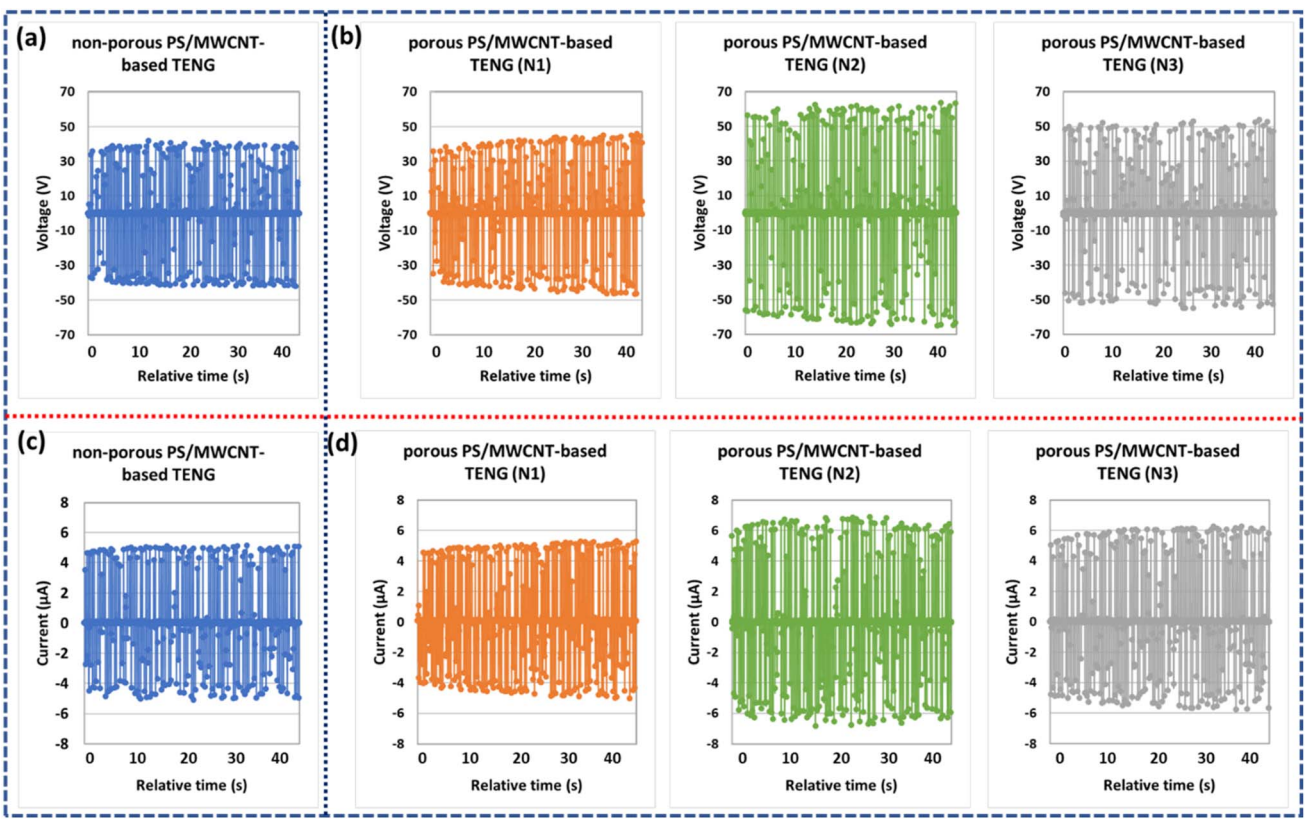

Fig. 9 Electrical output performance of TENG devices. (a) Open-circuit voltage of the non-porous PS/MWCNT nanocomposite-based TENG; (b) open-circuit voltage of the porous PS/MWCNT nanocomposite-based TENG; (c) short-circuit current of the non-porous PS/MWCNT nanocomposite-based TENG; (d) short-circuit current of the porous PS/MWCNT nanocomposite-based TENG.

shown in Fig. 9b and d, the porous films—labeled N1, N2, and N3—correspond to structures with fine, medium, and large pore sizes, respectively, controlled by the particle size of the sieved salt used as the sacrificial porogen.

The N1-based TENG, with fine porosity, exhibited modest improvement, reaching a maximum voltage of 46 V and a current of 5.3 μA. While performance was superior to the non-porous device, the limited enhancement may be due to the relatively small pore size, which could restrict local mechanical deformation and reduce the potential for charge separation. Moreover, finer pores may offer insufficient modulation of the bulk dielectric constant and interfacial charge trapping capability.

The highest triboelectric performance was obtained from the N2 sample, featuring a medium-sized porous structure. This device achieved a peak voltage of 65 V and a current of 6.9 μA—an increase of approximately 62.5% and 41% in voltage and current, respectively, compared to the non-porous counterpart. This substantial enhancement can be attributed to a synergistic interplay between several factors: increased real contact area due to uniform pore distribution, improved dielectric response through local electric field amplification, and enhanced charge localization at the interface between the triboelectric layers.

The N3-based TENG, with the largest pores among the samples, generated a voltage of 54 V and a current of 6.2 μA. Although its performance exceeded that of the non-porous and fine-porous devices, it was slightly lower than that of the N2 sample. This suggests that excessively large pores may compromise structural integrity, introduce mechanical softness, and lead to incomplete surface contact during operation. Such effects could diminish charge transfer efficiency despite the increased air-dielectric interface.

These findings underscore the importance of optimizing pore size and distribution to maximize triboelectric output. The medium-pore-size architecture of the N2 film likely provides the most favorable balance between surface roughness, mechanical compliance, dielectric modulation, and interfacial polarization. This configuration appears to promote efficient dipole orientation and robust charge separation under repeated mechanical excitation. Furthermore, the observed increase in current across all porous samples points to improved charge transfer kinetics. This is potentially facilitated by enhanced interfacial polarization, better stress distribution, and the presence of MWCNTs, which contribute to localized field enhancement and more effective charge transport pathways within the nanocomposite matrix.

Overall, these results validate the efficacy of the salt leaching approach as a simple, cost-effective, and scalable method for tuning the microstructure of dielectric layers in TENGs. The ability to tailor porosity without the need for complex lithographic or microfabrication techniques presents a significant advantage for the development of high-performance, flexible, and wearable energy harvesting systems.

To further evaluate the energy harvesting ability of the fabricated TENGs, the output power was calculated by multiplying the measured maximum open-circuit voltage and short-circuit current (Fig. 10). Although this method does not consider impedance matching external loads, it functions as a comparative measure to assess how porosity affects performance across different nanocomposite samples.

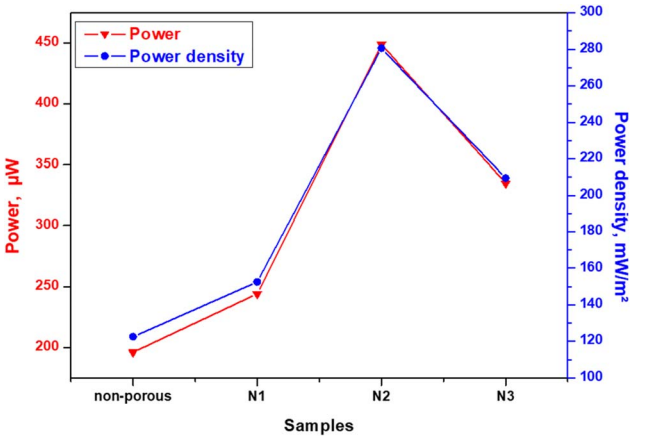

Fig. 10 Power and power density of TENGs based on porous PS/MWCNT nanocomposite films.

The non-porous PS/MWCNT-based TENG produced an output power of approximately 196 μW, representing the baseline condition. Upon introducing porosity, a noticeable enhancement in power output was observed. The fine-porous sample (N1) generated 244 μW, while the large-porous sample (N3) yielded 335 μW. The medium-porous sample (N2) exhibited the highest output power, reaching 449 μW. These results indicate that the integration of controlled porosity into the nanocomposite films significantly enhances the energy harvesting capability of the TENG devices. The superior performance of the N2 sample can be attributed to its balanced microstructure, which provides optimized contact area, mechanical compliance, and dielectric behavior, facilitating more effective charge generation and transfer.

To enable a more meaningful comparison across devices with the same geometry and to provide a parameter relevant for practical applications, the power density of each TENG was calculated by dividing the output power by the contact area of the device. All samples had a contact area of 4 cm × 4 cm, corresponding to 16 cm^2 or 1.6×10^{-3} m^2.

The calculated power density for the non-porous TENG was 122.5 mW m^{-2}. For the porous samples, the power densities were found to be 152.5 mW m^{-2} for N1 (fine-porous), 280.6 mW m^{-2} for N2 (medium-porous), and 209.4 mW m^{-2} for N3 (large-porous). These results further confirm that the medium-porous structure (N2) delivers the best performance, achieving more than twice the power density of the non-porous device.

The increased power density is attributed to enhanced triboelectric interactions enabled by the porous architecture. Specifically, the medium-sized pores promote improved surface roughness, increased real contact area, and more efficient dielectric response, all of which contribute to higher charge generation efficiency. These findings highlight the effectiveness of the salt leaching method in tuning the microstructure of nanocomposite films and underline the critical role of pore size in maximizing energy output in TENG.

The observed enhancement in TENG performance with porous PS/MWCNT films arises from a synergistic interplay of factors. The introduction of porosity increases the effective contact area and surface roughness, facilitating greater triboelectric charge generation. Simultaneously, the pores create localized dielectric contrasts and voids that act as charge trapping sites, enhancing surface charge density. Moreover, the mechanical compliance of the porous films improves contact intimacy during the contact – separation process, thereby promoting more efficient charge transfer. Collectively, these mechanisms – enhanced charge trapping, optimized surface contact, and tunable dielectric behavior – contribute to the substantial increase in voltage, current, and power density observed in the porous TENG devices.

4. Conclusion

In this study, porous PS/MWCNT nanocomposite films were fabricated using a salt leaching approach and employed as active dielectric layers in TENGs. The influence of pore size on the dielectric properties and output performance of the TENGs was systematically evaluated. Dielectric measurements revealed that increasing porosity led to a reduction in the dielectric constant, consistent with effective medium theory, due to the incorporation of low-permittivity air voids. Despite this reduction, the presence of MWCNTs and tailored porosity enabled enhanced charge localization and interfacial polarization. Triboelectric measurements demonstrated that TENGs with medium-sized pores exhibited the highest performance, achieving a maximum open-circuit voltage of 65 V, a short-circuit current of 6.9 μA, and a power density of 280.6 mW m^{-2}. This enhancement is attributed to the optimal combination of mechanical compliance, increased real contact area, and effective modulation of the dielectric environment, which together facilitated more efficient charge separation and transfer. These findings highlight the effectiveness of pore structure engineering as a powerful tool for tuning the electrical and dielectric performance of polymer-based TENGs. The results also confirm that medium-scale porosity in PS/MWCNT nanocomposites offers a promising strategy for the development of high-performance, low-cost, and flexible energy-harvesting devices suitable for wearable and self-powered electronics.

Author contributions

Orkhan Gulahmadov conceptualized the research and prepared the initial draft of the manuscript. Lala Gahramanli performed dielectric measurements, analyzed the data, and contributed to the interpretation of the Raman spectroscopy results. Nadia Todorova conducted the SEM characterization of the samples. Mustafa Muradov provided intellectual guidance and supervised the research workflow. Nahida Musayeva was responsible for recording and processing the Raman spectra of the nanocomposites. Christos Trapalis supported material preparation and contributed to the experimental methodology. Stefano Bellucci provided scientific oversight, critically reviewed the manuscript, and participated in its revision and final editing. All authors have read and approved the final version of the manuscript.

Conflicts of interest

The authors declare that they have no conflict of interest.

Data availability

The data presented in this study are available upon reasonable request from the corresponding author.

Acknowledgements

This research received no external funding. This research was partially supported by COST Action CA20126 – Network for research, innovation and product development on porous semiconductors and oxides (NETPORE). The authors gratefully acknowledge the network's contribution in facilitating scientific exchange and collaborative opportunities essential for carrying out this study.

References

1 C. C. Zhang, M. Y. Liu, S. Y. Han, A. Sedaghat, K. Zhang, and H. Wang, *Wearable Sensors and Devices: Enhancing Human Life*, 2025.
2 N. Niknejad, W. B. Ismail, A. Mardani, H. Liao and I. Ghani, A comprehensive overview of smart wearables: the state of the art literature, recent advances, and future challenges, *Eng. Appl. Artif. Intell.*, 2020, **90**, 103529.
3 Y. G. Park, S. Lee and J. U. Park, Recent progress in wireless sensors for wearable electronics, *Sensors*, 2019, **19**(20), 4353.
4 C. Y. Kim, J. Lee, E. Y. Jeong, Y. Jang, H. Kim, B. Choi, *et al.*, Wireless technologies for wearable electronics: a review, *Adv. Electron. Mater.*, 2025, **11**(2), 2400884.
5 M. S. Iqbal, H. Lu, S. Khaladkar, X. Wu, S. Roy, Z. Ullah and B. Guo, Recent advances in triboelectric nanogenerators: mechanism, rational designing and applications, *Mater. Today Energy*, 2024, **46**, 101732.
6 Z. Shi, Y. Zhang, J. Gu, B. Liu, H. Fu, H. Liang and J. Ji, Triboelectric nanogenerators: state of the art, *Sensors*, 2024, **24**(13), 4298.
7 T. Cheng, J. Shao and Z. L. Wang, Triboelectric nanogenerators, *Nat. Rev. Methods Primers*, 2023, **3**(1), 39.
8 C. Wu, A. C. Wang, W. Ding, H. Guo and Z. L. Wang, Triboelectric nanogenerator: a foundation of the energy for the new era, *Adv. Energy Mater.*, 2019, **9**(1), 1802906.
9 O. Gulahmadov, M. B. Muradov, L. Gahramanli, A. Karimova, S. Mammadyarova, S. Belluci and J. Kim, Development of Nylon/Fe3O4 Nanocomposite Triboelectric Nanogenerators for Self-Powered Transmission Line Monitoring Applications, *Energy Environ. Mater.*, 2025, **8**(3), e12880.

10 O. Gulahmadov, M. B. Muradov and J. Kim, Gait analysis by using electric signals from a triboelectric nanogenerator, *Eng. Res. Express*, 2022, **4**(3), 035027.
11 F. Ma, Y. Wu, S. Dai, P. Lin, J. Sun and L. Dong, A soft-contact hybrid electromagnetic–triboelectric nanogenerator for self-powered water splitting towards hydrogen production, *Nano Res.*, 2024, **17**(7), 6567–6574.
12 J. Wang, P. Li, X. Kang, Z. Li and S. Dai, Soft-soft contact TENG using nonlinear coupling galloping phenomenon for harvesting wind energy, *Nano Energy*, 2025, **133**, 110471.
13 W. Zhang, W. He, S. Dai, F. Ma, P. Lin, J. Sun, L. Dong and C. Hu, Wave energy harvesting based on multilayer beads integrated spherical TENG with switch triggered instant discharging for self-powered hydrogen generation, *Nano Energy*, 2023, **111**, 108432.
14 W. G. Kim, D. W. Kim, I. W. Tcho, J. K. Kim, M. S. Kim and Y. K. Choi, Triboelectric nanogenerator: Structure, mechanism, and applications, *ACS Nano*, 2021, **15**(1), 258–287.
15 S. Niu and Z. L. Wang, Theoretical systems of triboelectric nanogenerators, *Nano Energy*, 2015, **14**, 161–192.
16 O. Gulahmadov, M. B. Muradov and J. Kim, The wind-driven Scotch yoke-based triboelectric nanogenerator system for energy harvesting, *Int. J. Energy Res.*, 2022, **46**(8), 10989–10997.
17 B. Zhang, R. Wang, R. Wang, B. Chen, H. Li, A. Shen and Y. Mao, Recent advances in stretchable hydrogel-based triboelectric nanogenerators for on-skin electronics, *Mater. Chem. Front.*, 2024, **8**, 4003–4028.
18 F. R. Fan, W. Tang and Z. L. Wang, Flexible nanogenerators for energy harvesting and self-powered electronics, *Adv. Mater.*, 2016, **28**(22), 4283–4305.
19 A. Chen, C. Zhang, G. Zhu and Z. L. Wang, Polymer materials for high-performance triboelectric nanogenerators, *Adv. Sci.*, 2020, **7**(14), 2000186.
20 Y. Shang, Z. Wang, C. Yu, W. Xu, Z. Chen, B. Jiang and H. Zhang, Chemical structure-based design of triboelectric materials for high-performance TENGs, *Nano Energy*, 2022, **103**, 107847.
21 Z. Zhao, L. Zhou, S. Li, D. Liu, Y. Li, Y. Gao and Z. L. Wang, Selection rules of triboelectric materials for direct-current triboelectric nanogenerator, *Nat. Commun.*, 2021, **12**(1), 4686.
22 J. Kim, O. Gulahmadov and M. B. Muradov, Enhancement of performance of triboelectric generators by introduction of micro-and nano-structures on triboelectric films, *J. Mater. Sci.: Mater. Electron.*, 2021, **32**(20), 24661–24680.
23 Y. Yu, H. Li, D. Zhao, Q. Gao, X. Li, J. Wang and T. Cheng, Material's selection rules for high performance triboelectric nanogenerators, *Mater. Today*, 2023, **64**, 61–71.
24 R. Zhang and H. Olin, Material choices for triboelectric nanogenerators: A critical review, *EcoMat*, 2020, **2**(4), e12062.
25 J. E. Mark, Some interesting things about polysiloxanes, *Acc. Chem. Res.*, 2004, **37**(12), 946–953.
26 J. A. González Calderón, D. Contreras López, E. Pérez and J. Vallejo Montesinos, Polysiloxanes as polymer matrices in biomedical engineering: Their interesting properties as the reason for the use in medical sciences, *Polym. Bull.*, 2020, (5), 2749–2781.
27 A. S. Miroshnichenko, V. Neplokh, I. S. Mukhin and R. M. Islamova, Silicone materials for flexible optoelectronic devices, *Materials*, 2022, **15**(24), 8731.
28 J. Wang, J. Zhou, K. Jin, L. Wang, J. Sun and Q. Fang, A new fluorinated polysiloxane with good optical properties and low dielectric constant at high frequency based on easily available tetraethoxysilane (TEOS), *Macromolecules*, 2017, **50**(23), 9394–9402.
29 Y. Sheima, Y. Yuts, H. Frauenrath and D. M. Opris, Polysiloxanes modified with different types and contents of polar groups: Synthesis, structure, and thermal and dielectric properties, *Macromolecules*, 2021, **54**(12), 5737–5749.
30 E. R. Radu, D. M. Panaitescu, L. Andrei, F. Ciuprina, C. A. Nicolae, A. R. Gabor and R. Truşcă, Properties of polysiloxane/nanosilica nanodielectrics for wearable electronic devices, *Nanomaterials*, 2021, **12**(1), 95.
31 P. Moni, M. Wilhelm and K. Rezwan, The influence of carbon nanotubes and graphene oxide sheets on the morphology, porosity, surface characteristics and thermal and electrical properties of polysiloxane derived ceramics, *RSC Adv.*, 2017, **7**(60), 37559–37567.
32 S. Jabeen, A. Kausar, B. Muhammad, S. Gul and M. Farooq, A review on polymeric nanocomposites of nanodiamond, carbon nanotube, and nanobifiller: structure, preparation and properties, *Polym.-Plast. Technol. Eng.*, 2015, **54**(13), 1379–1409.
33 T. Tene, O. Gulahmadov, L. Gahramanli, M. Muradov, J. B. Gilev, T. Hamzayeva and C. Vacacela Gomez, Influence of MWCNT concentration on performance of Nylon/MWCNT nanocomposite-based triboelectric nanogenerators fabricated *via* spin coating method, *Nanoenergy Adv.*, 2025, **5**(3), 9.
34 A. Kausar, I. Rafique and B. Muhammad, Review of applications of polymer/carbon nanotubes and epoxy/CNT composites, *Polym.-Plast. Technol. Eng.*, 2016, **55**(11), 1167–1191.
35 E. A. Golovenko, D. V. Pankin, K. V. Deriabin, S. O. Kirichenko, I. Perevyazko, A. V. Koroleva and R. M. Islamova, Modified with ferrocenyl-containing oligo- and polysiloxanes multi-walled carbon nanotubes for soft conductive silicone composites, *Mater. Today Commun.*, 2024, **41**, 110429.
36 J. Marchewka, P. Jeleń, E. Długoń, M. Sitarz and M. Błażewicz, Spectroscopic investigation of the carbon nanotubes and polysiloxane coatings on titanium surface, *J. Mol. Struct.*, 2020, **1212**, 128176.
37 M. Chodkowski, I. Y. Sulym, K. Terpiłowski and D. Sternik, Surface properties of silica–MWCNTs/PDMS composite coatings deposited on plasma activated glass supports, *Appl. Sci.*, 2021, **11**(19), 9256.
38 A. Mahapatra, R. S. Ajimsha, D. Deepak, R. Aggarwal, S. Kumar, R. Venkatesh, S. Sinha Roy and P. Misra, Textile-integrated MoS2-PDMS single electrode triboelectric nanogenerator for vibrational energy harvesting and

biomechanical motion sensing, *Nano Energy*, 2023, **116**, 108829.

39 X. Xia, J. Chen, G. Liu, M. S. Javed, X. Wang and C. Hu, Aligning graphene sheets in PDMS for improving output performance of triboelectric nanogenerator, *Carbon*, 2017, **111**, 569–576.

40 D. Tantraviwat, M. Ngamyingyoud, W. Sripumkhai, P. Pattamang, G. Rujijanagul and B. Inceesungvorn, Tuning the dielectric constant and surface engineering of a BaTiO3/Porous PDMS composite film for enhanced triboelectric nanogenerator output performance, *ACS Omega*, 2021, **6**(44), 29765–29773.

41 Z. Liu, M. Muhammad, L. Cheng, E. Xie and W. Han, Improved output performance of triboelectric nanogenerators based on polydimethylsiloxane composites by the capacitive effect of embedded carbon nanotubes, *Appl. Phys. Lett.*, 2020, **117**(14), 142903.

42 H. Jamil, M. Faizan, M. Adeel, T. Jesionowski, G. Boczkaj and A. Balčiūnaitė, Recent advances in polymer nanocomposites: unveiling the frontier of shape memory and self-healing properties—a comprehensive review, *Molecules*, 2024, **29**(6), 1267.

43 Z. Duan, F. Cai, Y. Chen, T. Chen and P. Lu, Advanced applications of porous materials in triboelectric nanogenerator self-powered sensors, *Sensors*, 2024, **24**(12), 3812.

44 Y. Peng, K. Wang, M. Yu, A. Li and R. K. Bordia, An optimized process for *in situ* formation of multi-walled carbon nanotubes in templated pores of polymer-derived silicon oxycarbide, *Ceram. Int.*, 2017, **43**(4), 3854–3860.

45 Z. Turar, M. Sembay, A. Mubarak, A. Belgibayeva, L. Kong and G. Kalimuldina, Advances in porous structure design for enhanced piezoelectric and triboelectric nanogenerators: A comprehensive review, *Glob. Chall.*, 2025, **9**(1), 2400224.

46 C. Pinming, W. Wongwiriyapan, S. Rattanamai, N. Ketama, A. Treetong, T. Ikuno and A. Klamchuen, Carbon nanotube/polydimethylsiloxane composite micropillar arrays using non-lithographic silicon nanowires as a template for performance enhancement of triboelectric nanogenerators, *Nanotechnology*, 2020, **32**(9), 095303.

47 L. Luo, B. Zhang, Y. Lei, D. Chai, D. Zhang, K. Xu and H. Wang, Interface-engineered porous PDMS-MWCNTs composites through HPC-mediated "sponge pump absorption" strategy for high-performance triboelectric nanogenerators, *Mater. Today Commun.*, 2025, **44**, 112192.

48 O. Gulahmadov, M. B. Muradov, H. Mamedov and J. Kim, Enhancement of triboelectric nanogenerators with nylon/TiO2 nanocomposite films, *MRS Commun.*, 2024, **14**(1), 114–120.

49 O. Gulahmadov, L. Gahramanli, M. Muradov, H. Mamedov, A. Musayev, C. V. Gomez and S. Bellucci, Investigating the effect of variation of TiO_2 nanoparticle concentration on the performance of nylon/TiO_2 nanocomposite-based TENG, *J. Ovonic Res.*, 2024, **20**(6), 831–839.

50 O. Gulahmadov, L. Gahramanli, M. Muradov, N. Musayeva, J. B. Gilev and S. Bellucci, Fabricating nylon/multiwalled carbon nanotube (MWCNT) nanocomposites for potential use in triboelectric nanogenerators (TENGs), *Fullerenes, Nanotubes Carbon Nanostruct.*, 2025, **33**(8), 833–842.

51 O. Gulahmadov, L. Gahramanli, M. Muradov, J. B. Gilev, S. Bellucci and C. Vacacela Gomez, Optimization of MWCNT concentration in nylon-based nanocomposites for enhanced triboelectric nanogenerator performance, *J. Mater. Sci.:Mater. Electron.*, 2025, **20**(1), 101.

52 G. C. Patil, Doctor blade: a promising technique for thin film coating, in *Simple Chemical Methods for Thin Film Deposition: Synthesis and Applications*, Springer Nature Singapore, Singapore, 2023, pp. 509–530.

53 M. A. Butt, Thin-film coating methods: a successful marriage of high-quality and cost-effectiveness—A brief exploration, *Coatings*, 2022, **12**(8), 1115.

54 **https://www.ossila.com/pages/solution-processing-techniques-comparison#doctor-blade-coating**.

55 Y. Jiao, Z. Lin, X. Ma, L. Zhou, X. Guo, Z. Hu and J. Chang, High-performance triboelectric nanogenerators based on blade-coating lead halide perovskite film and electrospinning PVDF/graphene nanofiber, *Chem. Eng. J.*, 2024, **483**, 149442.

56 S. R. Srither, N. R. Dhineshbabu, D. S. Shankar Rao, S. Krishna Prasad, O. Dahlsten and S. Bose, Transparent Triboelectric Nanogenerator Based on Thermoplastic Polyurethane Films, *J. Nanosci. Nanotechnol.*, 2021, **21**(5), 3072–3080.

57 Q. Hou, D. W. Grijpma and J. Feijen, Porous polymeric structures for tissue engineering prepared by a coagulation, compression moulding and salt leaching technique, *Biomaterials*, 2003, **24**(11), 1937–1947.

58 Y. Zou, J. Xu, K. Chen and J. Chen, Advances in nanostructures for high-performance triboelectric nanogenerators, *Adv. Mater. Technol.*, 2021, **6**(3), 2000916.

59 D. Ryoo, J. Y. Kim, P. K. Duy, S. H. Cho, H. Chung and T. H. Yoon, Fast and non-destructive Raman spectroscopic determination of multi-walled carbon nanotube (MWCNT) contents in MWCNT/polydimethylsiloxane composites, *Analyst*, 2018, **143**(18), 4347–4353.

60 L. Jayes, A. P. Hard, C. Séné, S. F. Parker and U. A. Jayasooriya, Vibrational spectroscopic analysis of silicones: A Fourier transform-Raman and inelastic neutron scattering investigation, *Anal. Chem.*, 2003, **75**(4), 742–746.

61 V. Borjanović, L. Bistričić, I. Vlasov, K. Furić, I. Zamboni, M. Jakšić and O. Shenderova, Influence of proton irradiation on the structure and stability of poly(dimethylsiloxane) and poly(dimethylsiloxane)-nanodiamond composite, *J. Vac. Sci. Technol. B*, 2009, **27**(6), 2396–2403.

62 A. D. Dobrzańska-Danikiewicz, W. Wolany, D. Łukowiec, K. Jurkiewicz and P. Niedziałkowski, Characteristics of multiwalled carbon nanotubes-rhenium nanocomposites with varied rhenium mass fractions, *Nanomater. Nanotechnol.*, 2017, **7**, 1847980417707173.

63 W. Duan, D. Jia, D. Cai, B. Niu, Z. Yang and Y. Zhou, Effects of pore structures on the dielectric properties of silicon

nitride-based ceramics, *J. Eur. Ceram. Soc.*, 2020, **40**(15), 6223–6228.

64 H. Chen, and Z. Heidari, Pore-scale evaluation of dielectric measurements in formations with complex pore and grain structures, in *SPWLA Annual Logging Symposium*, SPWLA, 2014, p. SPWLA-2014.

65 J. K. Nayak, P. Roy Chaudhuri, S. Ratha and M. R. Sahoo, A comprehensive review on effective medium theories to find effective dielectric constant of composites, *J. Electromagn. Waves Appl.*, 2023, **37**(2), 282–322.

66 Z. Hou, F. Ye and L. Liu, Effects of pore shape and porosity on the dielectric constant of porous β-SiAlON ceramics, *J. Eur. Ceram. Soc.*, 2015, **35**(15), 4115–4120.

67 Z. Azizoglu, and Z. Heidari, Interpretation of multi-frequency dielectric permittivity measurements for assessment of water saturation in carbonate formations with complex pore structure, in *SPWLA Annual Logging Symposium*, SPWLA, 2021, p. D021S011R002.

68 H. Y. Mi, X. Jing, Z. Cai, Y. Liu, L. S. Turng and S. Gong, Highly porous composite aerogel based triboelectric nanogenerators for high performance energy generation and versatile self-powered sensing, *Nanoscale*, 2018, **10**(48), 23131–23140.

69 Z. Bai, Y. Xu, Z. Zhang, J. Zhu, C. Gao, Y. Zhang and J. Guo, Highly flexible, porous electroactive biocomposite as attractive tribopositive material for advancing high-performance triboelectric nanogenerator, *Nano Energy*, 2020, **75**, 104884.

70 Y. Mi, Z. Zhao, H. Wu, Y. Lu and N. Wang, Porous polymer materials in triboelectric nanogenerators: a review, *Polymers*, 2023, **15**(22), 4383.

71 Z. Saadatnia, S. G. Mosanenzadeh, E. Esmailzadeh and H. E. Naguib, A high performance triboelectric nanogenerator using porous polyimide aerogel film, *Sci. Rep.*, 2019, **9**(1), 1370.